ADVANCED MATERIALS TECHNOLOGIES
www.advmattechnol.de

Advective Assembler-Enhanced Support Bath Rotational Direct Ink Writing

*Tazio Pleij, Alexandra V. Bayles, and Jan Vermant**

Manufacturing intricately controlled, hierarchically distributed structures poses significant fabrication challenges, but is crucial for enhancing functionality in synthetic systems. A 3D printing technique combining advective assembly with rotational direct ink writing is developed and exploited to build topologically complex, multimaterial structures with high precision. A modular advective assembler printhead is fabricated and employed in the process. This flow-structuring device is designed with a complex network of internal channels that patterns flowing hydrogel-based inks, creating multi-layered filaments whose structures go well beyond conventional nozzle shape and size limitations. The composite filaments are extruded into a rotating support bath of Polyacrylic acid microgels. The rheology of the inks and support bath are critical to maintain print fidelity and integrity, and are characterized by linear and nonlinear bulk rheometry. Optimization of the materials creates a platform where curvilinear, multimaterial architectures are constructed without being constrained to slicing across X, Y, and Z axes. The versatility of this manufacturing platform is demonstrated by printing helical structures that undergo swelling-induced actuation. This processing method has the potential to significantly enhance additive manufacturing by enabling the production of intricate, multiscale composite structures with broad applicability in fields such as bioengineering, soft robotics, and functional composite materials.

1. Introduction

Functionality in materials can be enhanced by internal composition gradients and hierarchical architectures. Examples from nature include structured keratinous materials such as nails and feathers,[1] sunflower stems where the arrangement of phases in the pith parenchyma controls the plant's hydrostatic motor behavior,[2] and ice plant seeds with precise distributions of swellable cellulose layers responsible for its origami-like unfolding.[3] Unlike nature's resource-efficient designs, creating synthetic structures with organized phases across multiple hierarchical levels in a scalable way remains a challenge.

3D printing or additive manufacturing (AM) processes have revolutionized the manufacturing and design industry by enabling the fast and customized production of complex 3D objects. 3D printing has numerous advantages ranging from rapid prototyping, design flexibility, and customization of manufactured objects to the minimization of waste material. However, most AM techniques are ill-suited to create composition gradients or hierarchical structures, as they impose stringent constraints on materials used. For example, fused deposition modeling is limited to employing thermoplastic filaments, while stereolithographic light processing methods are limited to photo-curable resins or polymers. In this respect, an exception amongst 3D printing methodologies is direct ink writing (DIW), a simple AM process that involves the controlled extrusion of materials,[4] often referred to as inks. DIW differentiates itself from other AM technologies due to its versatility, as it is not restricted to a single material or class of materials.[5] Rather, DIW can utilize any precursor formulation, provided that the ink exhibits suitable rheological characteristics,[6] which include a finite zero-shear viscosity, sufficient shear thinning, a fast structural recovery after deposition and solid-like behavior at rest.[7,8]

One limitation of conventional DIW printing systems is that they must construct objects layer-by-layer which restricts the complexity of vertically spanning structures. Some approaches to overcome this constraint use removable support structures,[9,10] but one of the most promising strategy is support bath-assisted or embedded 3D printing. In this technique, inks are extruded into a high-yield-stress fluid known as the "support bath". The support bath is deformable at appreciably high shear, allowing the nozzle to translate freely, but it is also recoverable, allowing the fluid to encase printed structures and support them against gravity. After the printed structure has been solidified, the

T. Pleij, J. Vermant
Department of Materials
ETH Zürich
Zürich CH-8093, Switzerland
E-mail: jan.vermant@mat.ethz.ch
A. V. Bayles
Department of Chemical and Biomolecular Engineering
University of Delaware
Newark, DE 19716, USA

The ORCID identification number(s) for the author(s) of this article can be found under https://doi.org/10.1002/admt.202400005

© 2024 The Authors. Advanced Materials Technologies published by Wiley-VCH GmbH. This is an open access article under the terms of the Creative Commons Attribution License, which permits use, distribution and reproduction in any medium, provided the original work is properly cited.

DOI: 10.1002/admt.202400005

support bath can be removed in a post-processing step. This method enhances DIW capabilities by enabling omnidirectional printing and allows for the use of inks with reduced viscosity, storage modulus, and yield stress. It has been extensively studied for materials like polydimethylsiloxane-based inks[11,12] and cell-laden hydrogels for tissue engineering applications.[13,14] In the vast majority of support-bath demonstrations, a single ink formulation is used to construct the object.

Separately, multimaterial additive manufacturing has been developed to create composite objects with enhanced properties and functionality. One common approach to print structures composed of distinct materials involves using multiple DIW nozzles to sequentially extrude different inks.[15–18] This method significantly advanced multimaterial AM, but it has drawbacks such as prolonged printing times due to frequent nozzle switching. Additionally, there is often poor adhesion both between layers of the same material and between different materials, leading to compromised mechanical properties and performance, such as electrical contact loss in sensors or actuators.[19] Hence, this approach often requires additional post-processing steps.

An alternative approach to building 3D multimaterial structures via DIW involves customizing the printing nozzle to shape structures within the extruded flow. These extrusion-based AM methods have gained attention for their ability to precisely control multimaterial arrangements at scales below the nozzle size (subvoxel),[20,21] to print multiple filaments in parallel,[22] or to quickly switch in-line between different types of ink being extruded.[23–25] Printheads designed to co-extrude structured filaments mainly focused on bi-phasic and coaxial configurations[26–28]. Recently, research has shifted toward rotational DIW printing methods where specialized printheads co-extrude multimaterial filaments during rotation of the printhead itself.[29,30] This approach provides precise control over azimuthal variations within helical multimaterial filaments, enabling the creation of intricate and versatile structures.

Advective assemblers are a particular class of co-extrusion printheads capable of building designer filament structures with remarkable efficiency. Whereas most co-extrusion nozzles extrude inks through a narrow shaped die, the advective assembly devices are composed of millimeter sized channels connected by splitting, rotating, and recombining T-junctions.[31] These junctions are combined in series to multiply laminar streamlines within the flow cross section.[32] The flows multiply architectures in a fractal-like manner, shrinking the characteristic dimension of architectural features at every replicate. These devices are similar to static mixers except that they use chaotic advection to build rather than to blend. Advective assemblers have been proven to be efficient at structuring material flows on different length scales and across various degrees of geometrical complexity.[33–35] Our recent work showcased the predictability and precision of this flow-patterning technique, demonstrating its capability to engineer even highly complex multiphase flow geometries.[36] Advective assembler printheads have been used to template the cross-linking density distribution of multi-phase hydrogel filaments and program actuation, all while maintaining exceptionally high throughput for an AM process.[37]

In the present work, we combine advective assembly printheads with rotational support-bath 3D printing to create complex architectures with smooth, curvilinear topologies. We demonstrate how it is possible to surpass the typical resolution limitations of the DIW techniques, which is usually dictated by the nozzle size, by now assembling patterns inside the nozzle, ahead of the support bath. To maintain pattern fidelity, we use inks with rheological behavior optimized for advective processing. By adjusting the ink type and flow rate in the flow-structuring printhead, we finely tune multi-inks cross-sectional geometry and patterning features. The combination of rotational and support-bath-assisted 3D printing expands spatial axes of design beyond X, Y, and Z dimensions, allowing for the construction of complex 3D objects that would be otherwise challenging to produce. As in natural materials, functionality is enhanced through structural hierarchy. We demonstrate this capability by building a library of helical structures with patterned cross-link distributions. We show how we can precisely program the differential swelling of biphasic helical structures by adjusting ink and print parameters, specifically the phase ratios, bilayer orientations, and macroscopic geometric aspects such as helical pitch and radius. This new printing platform expands the design toolbox with the added help of efficiency gains.

2. Approach

An E3D ToolChanger 3D printer was customized to house the advective assembler printhead shown in **Figure 1**. The printhead itself was fabricated by sterolithography 3D printing. Flows inside the printhead finely manipulate the internal structure of the extruded multimaterial filament, while the 3D printer controls the deposition process (using G-code). We integrated a rotational motor into the printbed to control the orientation of the support bath independently from the placement of the printhead. Combining the printhead flows, the position of the nozzle, and the rotation of the support bath provides unprecedented spatial printing freedom. Here, we use it to deposit the structured filaments vertically (in z-direction) without the need of printing any additional support structures.

Hydrogel inks are fed into the advective assembly printhead (see Figure 1) via PVC tubing connected to external syringe pumps (not shown). The distance between the dispensing pumps and inlets was minimized to reduce pressure drop and effects of tubing compliance. However, there were still noticeable delays in starting and stopping extrusion compared to the dispensing system inputs. Nevertheless, our independent control over each inlet's volumetric flow rate allowed us to precisely adjust the internal geometric distribution of phases within the extruded flow.

3. Results and Discussion

In this study, the advective assembler printhead used four inlets (labeled 1-4 in Figure 1b). The flow from inlets 1 and 2 is merged to form a tri-layer stream using a simple three-way addition junction. Following this, the flow is horizontally sectioned and the resulting streams undergo clockwise rotation before being recombined. This sequence is repeated twice, increasing the number of layers from three to nine. The inks from inlets 3 and 4 are then adjoined advectively, merging with the upper and lower portions of the stratified flow (left inserts in Figure 1). This advective assembler design was inspired by our previous work,[37] which showed

© 2024 The Authors. Advanced Materials Technologies published by Wiley-VCH GmbH

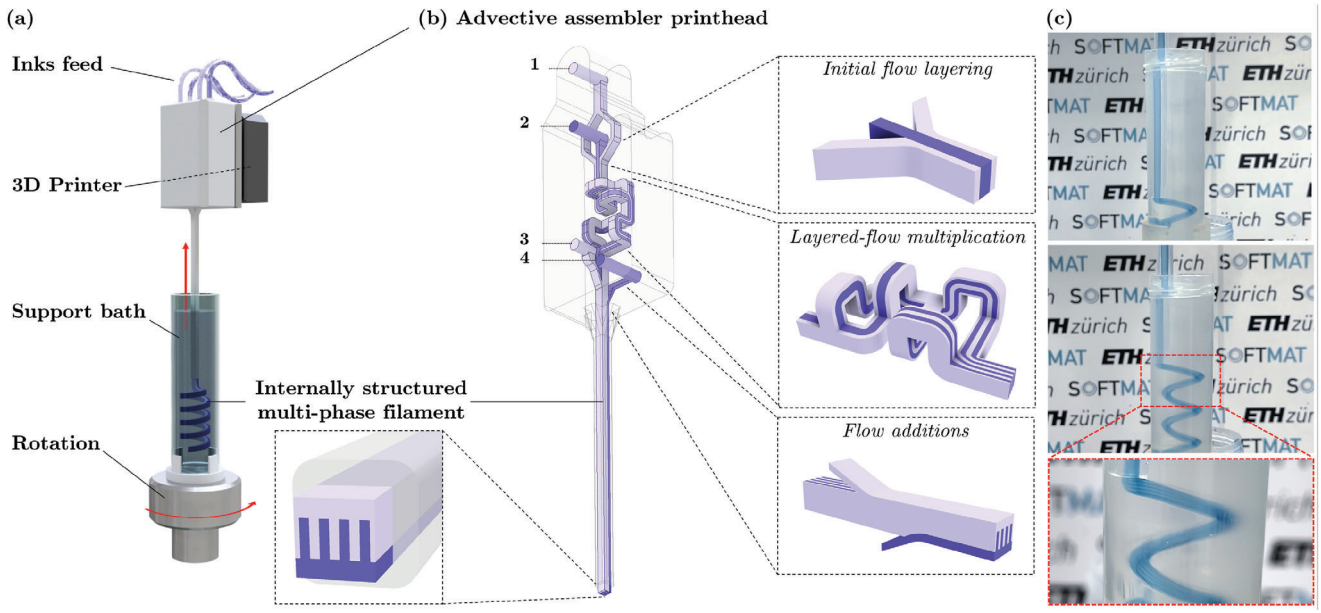

Figure 1. Rotational support bath-assisted advective direct ink writing setup. a) A custom 3D printer is equipped with an advective assembler printhead shown in detail in b) featuring internal rectangular channels. In this printhead, a three-layered flow from inlets 1 and 2 is transformed into a nine-layered flow. Additional streams from inlets 3 and 4 are then introduced, allowing for the creation of various flow geometries, such as the double-comb geometry shown here (3 mm x 3 mm extrudate dimension). External syringe pumps (not shown) independently control the flow rates of the four inlets. The structured flow is deposited into a support-bath fluid, facilitating vertical (z-direction) printing without supports. The extrudate is held in place within the high yield-stress support bath until it undergoes photo-polymerization. c) Still frames of advective printing process of a helical structure with internally structured, multi-inks filament (detail in the inset).

how a comb-structuring geometry improved interfacial adhesion between the two phases. The architecture looks and acts like interfacial Velcro, and it reduced delamination between the multiple materials when strained during swelling.

The add, split, and rotation junctions can be combined in different sequences to produce diverse architectures. In Figure 1a double comb geometry is depicted, serving only as one example. In a previous work, we developed a simple predictive framework based on Boolean logic to quickly design the internal filament structure. The modularity of the devices enables complex voxelated multi-phasic extrudate geometries, if needed, well beyond the double comb flow architecture studied here.

Following Bayles et al.[37] PAA-PEGDA hydrogel blends are used as DIW inks, with the dense PAA microgel suspension serving as a carrier yield stress fluid in which the PEGDA monomers are dissolved.[39] For the PEGDA concentrations and PAA volume fractions used, the microgels entirely dictate the inks rheological behavior. Flow curves measured over the shear rate range relevant for the process are shown in **Figure** 2a (average of triplicates, error-bars are smaller than the symbols size). These confirm the simple yield stress fluid nature of these materials, with solid properties at low stresses and shear-thinning beyond the critical stress. The yield stress causes the ink to flow as a plug through the twisting junctions and reliably template flow.[37] A simple constitutive equation for such materials is the Herschel-Bulkley model:

$$\tau = \tau_{y,static} + k \cdot \dot{\gamma}^{n} \quad (1)$$

with τ being the shear stress in Pa, $\tau_{y,\,static}$ the so-called static (or Herschel Bulkley) yield stress in Pa, k the consistency index in Pa·s^n, $\dot{\gamma}$ the shear rate in s^{-1} and n the dimensionless flow index. This relationship models the measurements well as evidenced by the R-squared values exceeding 0.9994 for all measured materials (see Table S1, Supporting Information). The 1.5 wt% PAA + 10 wt% PEGDA ink and the 1.5 wt% PAA + 20 wt% PEGDA inks display clear shear thinning behavior with flow indices of 0.430 ± 0.004 and 0.426 ± 0.005, respectively. The static yield stress ($\tau_{y,\,static}$) was obtained by extrapolating the Herschel-Bulkley fit to zero shear rate and characterizes the maximum elastic stress a fluid can carry under static conditions. Stress amplitude sweeps confirm the elastic behavior and moderate plateau storage modulus of inks (see Figure 2b).

Quantifying the yield stress of DIW inks is important as it ultimately defines the shape stability of the extruded filaments against gravitational slumping and capillary induced distortions.[40,41] For the two PAA-PEGDA inks, the static yield stress matched almost perfectly, similar to the other rheological parameters measured. The 10 wt% PEGDA ink showed $\tau_{y,\,static}$ = 100.3 ± 0.8 Pa ($G'_{plateau}$ = 493 ± 3 Pa), and the 20 wt% PEGDA ink exhibited $\tau_{y,\,static}$ = 91 ± 1 Pa ($G'_{plateau}$ = 493 ± 3 Pa).

To determine how fast the inks recover their solid-like behavior after extrusion from the printhead, we performed three interval thixotropy tests (see Figure S3c, Supporting Information). Both inks recover around 85% of their viscosity within 1 s after a considerable reduction in shearing conditions (sudden shear rate drop from 10 s^{-1} to 0.1 s^{-1}, and 100% of their reference viscosity is recovered within 23 s).

© 2024 The Authors. Advanced Materials Technologies published by Wiley-VCH GmbH

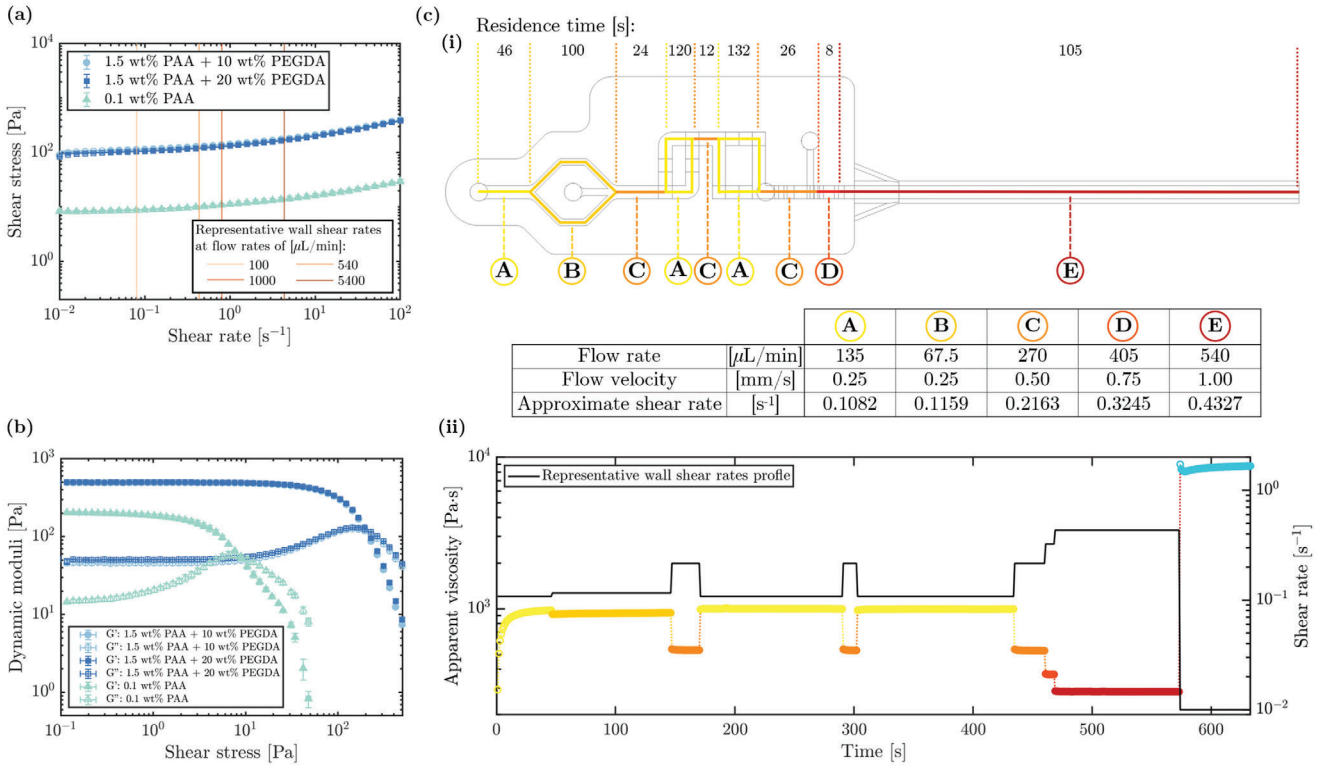

		A	B	C	D	E
Flow rate	[μL/min]	135	67.5	270	405	540
Flow velocity	[mm/s]	0.25	0.25	0.50	0.75	1.00
Approximate shear rate	[s⁻¹]	0.1082	0.1159	0.2163	0.3245	0.4327

Figure 2. Rheological characterization of inks and support bath. a) Flow curves, shear stress versus rate of PAA-PEGDA hydrogel inks (blue and light blue data) and PAA microgel support bath (green data). Open symbols represent data not acquired at steady state (see Figure S3a, Supporting Information) and were hence excluded from the fit. Lines show fit to Herschel-Bulkley model (fit parameters in Table S1, Supporting Information) with orange lines illustrating the approximate wall shear rate[38] at different net ink flow rates. b) Amplitude sweeps of inks and support bath performed at $\omega = 10$ rads^{-1}. c) Analysis of flow conditions inside of printhead during advective assembly. i) The printhead model is divided into five distinct shear conditions (A to E) that change as the flow is split or ink is added. Inks' residence times for a total flow rate of 540 μLmin^{-1} are displayed above the printhead model. Table with: flow rates, flow velocities, and wall shear rates for each shear section. ii) Processing shear rate profile, with shear rate displayed as a black line and ink viscosity represented by colored symbols corresponding to the shear condition sections. Blue data (viscosity at a shear rate of 0.01 s^{-1}) represents the post extrusion viscosity.

A more accurate depiction of shear rate conditions in our advective assembler printhead is displayed in Figure 2c. Here, we designed a shear rheometer protocol to replicate the exact shear conditions of a typical printing procedure (for a total flow rate at the outlet of 540 μLmin^{-1}). As the inks move through the advective assembler, shear stress imposed on them changes dynamically every time the flow is split, recombined or a new ink section is adjoined to the main stream (see Figure 2c (i)).

The rheological behavior of the fluids subjected to this process is shown in Figure 2c (ii). It reveals how the viscosity of the fluids responds to the different stress and residence times in the various parts of the device. This ability to respond rapidly to changes in shear stress is very important in the process to prevent flow instabilities that would disrupt the flow pattern. Increasing extrusion velocities would reduce the residence time but simultaneously increase shear stress. Since the velocity profiles deviate more from plug flow at higher stress[37] the stability of the coflowing layers is no longer ensured. The tradeoff between stability and shear rate imposes an upper limit on processing speeds.

The structured filaments were deposited into a 0.1 wt% PAA microgel solution support bath. In order to optimize the printing procedure, we carefully adjusted the yield stress and plateau storage modulus of the suspension bath. If the yield stress is too low, the extruded structures may slump or collapse toward the bottom of the support bath. On the other hand, if the yield stress is too high, the printhead nozzle would permanently displace the support bath as it moves through it, making it challenging to print vertically spanning structures with complex 3D geometries. The suspension bath showed $\tau_{y,\,static} = 7.5 \pm 0.1$ Pa and $G'_{plateau} = 200.3 \pm 3.0$ Pa. Both the yield stress and the shear elastic modulus of the support bath matrix are considerably smaller than that of the printed inks, indicating that the suspension media is ideal for embedded 3D printing.[42,43] Furthermore, we estimated the Oldroyd number *Od* which compares the yield stress of the support bath fluid with the flow stress of the extruded material, defined as:

$$Od = \frac{\tau_{y,static} \cdot d^n}{k \cdot U^n} \tag{2}$$

with d being the nozzle diameter, n and k being the power law exponent and the consistency index of the ink and U the extrusion velocity. For a typical printing procedure $Od \approx 3.65$. Following Grosskopf et al.[44] an $Od > 1$ is optimal for suspension bath printing, as long as the support bath material exhibits sufficiently fast self healing. Such a high *Od* implies that the volume of the

© 2024 The Authors. Advanced Materials Technologies published by Wiley-VCH GmbH

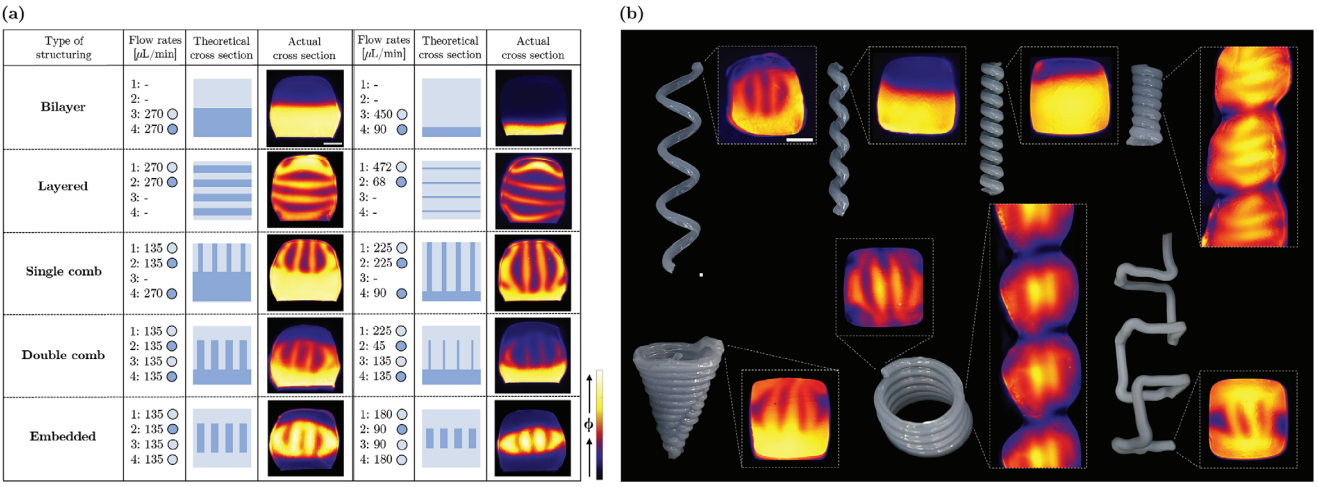

Figure 3. Cross-sectional geometry of advectively structured filaments and 3D-printed structures in a support bath. a) Five potential configurations of internal multi-phase filament structures achievable with the advective printhead, along with their flow rates and inks. Light blue represents the 1.5 wt% PAA + 10 wt% PEGDA ink (low ϕ-phase), while dark blue represents the 1.5 wt% PAA + 20 wt% PEGDA ink (high ϕ-phase). The predicted flow cross-sections for perfect plug flow are compared with fluorescent color maps depicting PEGDA volume fraction distributions (scale bar is 1 mm). b) Cross-linked 3D structures printed in the support bath, showing their internally structured, advectively assembled filament architecture. From left to right, top row: helix (radius 7.5 mm, pitch 20 mm) with an internal double comb structure, helix (radius 2.5 mm, pitch 10 mm) with 50/50 bilayer internal architecture, helix (radius 2.5 mm, pitch 5 mm) with 75/25 bilayer internal architecture, closed tubular structure (radius 5.5 mm) with horizontally oriented layered internal structure. Bottom row: inverted cone with single comb internal architecture, cylinder (radius 20 mm) with vertically oriented layered internal structure, linear squared structure, with inverted embedded phase filament's internal structure. This structure was printed by linearly moving the nozzle in all three directions through the support bath without any rotation. Scale bars (first structure and micrograph) are 1 mm.

yielded support bath material region around the moving nozzle is minimized, which improves overall print fidelity.

One feature of advective assembly support bath printing is that a single printhead can produce diverse structure by tuning simple processing parameters such as degree of rotation and relative flow rate. Structures produced by the four inlet comb printhead are shown in **Figure** 3a. The relative flow rate fed to the four inlets is varied while the total extrusion flow rate is maintained at 540 $\mu Lmin^{-1}$. Different combinations of inlets produce qualitatively different structures. For instance, using inlets 3 and 4 generates a simple bilayer profile; using only inlets 1 and 2 creates a nine-layered filament; using all four inlets creates a comb. Adjusting flow rates fine tunes thickness of features of the internal architecture.

The column on the left of Figure 3a shows the first order prediction of the structure, while the right shows experiments of the extruded filament. Multiple factors contribute to the filaments' structuring deviating from the perfectly orthogonal first-order prediction. First, the surface finish of the printhead's internal channels can lead to rounding of the internal features during assembly. This effect is especially noticeable in the nine-layered filament cross-sections (second row in Figure 3a), where the high ϕ-phase layers curve toward the sides due to channel roughness. Additionally, slight filament slumping after deposition can cause geometric distortions. The imaging process for multi-phase extrudate is challenging due to the brittleness of cross-linked hydrogels, making it hard to obtain uniform slices. Finally, the intense fluorescent signal from the high-ϕ phase can disturb the imaging, causing blurring of interfaces, and some inter-diffusion between phases prior to photopolymerization is expected with the inks used. Although these deviations may be problematic in applications where straight lines are valuable, we find them to be beneficial when making soft actuators. The diffuse, curved interfaces do not contain clean planes for delamination. For all of the actuators fabricated in this study, none delaminated under swelling-induced strain.

We selected different architectures to showcase our ability to print objects with complex 3D topographies with intricate internal architectures. Several emblematic examples are showcased in Figure 3b. Video recordings of the printing for most of these structures can be found in the Supporting Information.

Combining two layers with distinct swelling contrast leads to curling of the biphasic structure upon water exposure. This occurs because the layer with higher water absorption capacity (in this case the phase with lower PEGDA cross-linking density) expands more than its bonded counterpart. Although the differential-swelling behavior of flat or linear bilayers has been extensively explored,[45–49] its potential for more complex shape-morphing applications has not yet been pursued, as suitable and scalable processing techniques were lacking. Here, we exploit the potential for shape-morphing applications by printing helices with differing swelling behaviors using our advective support bath-assisted 3D printing technology. This allows us to precisely control both the geometric properties of the helices and the relative amounts of the two phases.

Figure 4 illustrates the swelling behavior of various helical structures when submerged in deionized water for 3 h. We show select frames from these recordings. Each column corresponds to a different sample and each row corresponds to a 10-min interval for 60 min. The images in Figure 4a (i)–(iv), compare the shape morphing of helical structures sharing identical macroscopic architecture (helical radius: 7.5 mm, helical pitch: 15 mm, height: 60 mm) but with different internal structure. Figure 4a (i) shows a helix composed solely of the 1.5 wt% PAA/10 wt%

© 2024 The Authors. Advanced Materials Technologies published by Wiley-VCH GmbH

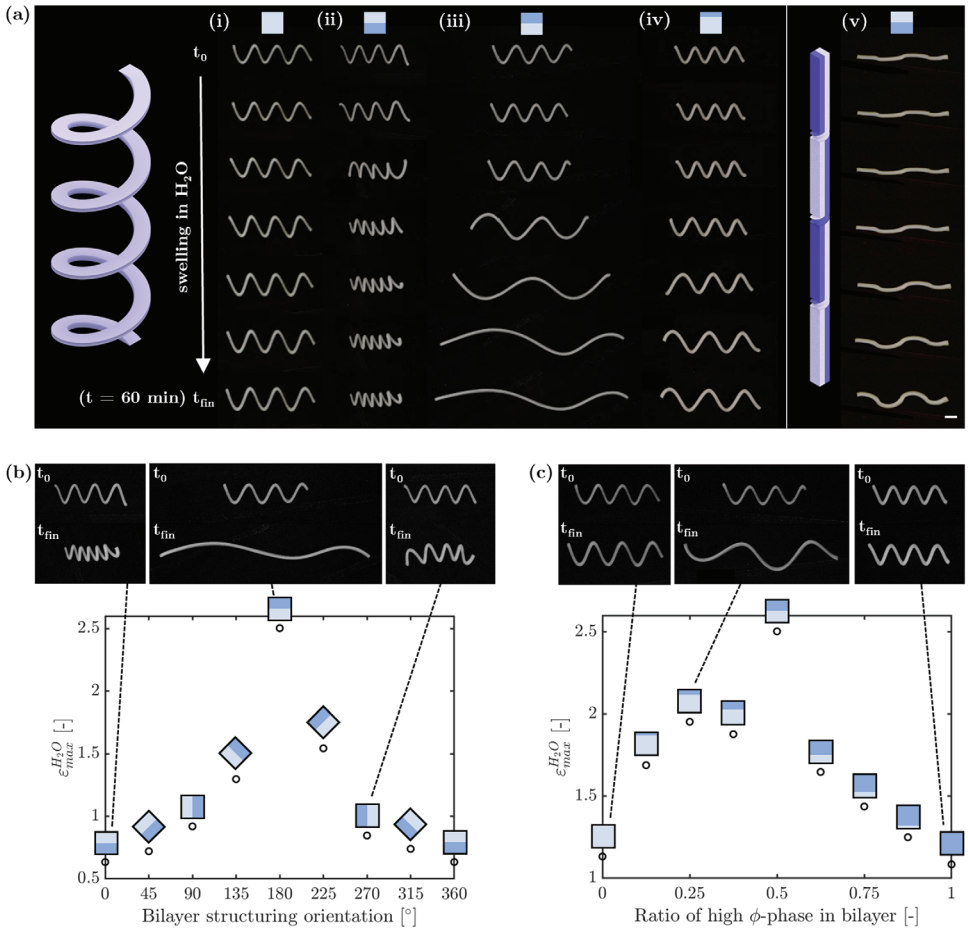

Figure 4. Shape changes of support-bath printed helicoidal bilayer-based structures. a) Top: filament internal multiphase architecture. i) homogeneous low ϕ-phase, ii) 50/50 structure low ϕ-phase on the exterior, iii) 50/50 bilayer with low ϕ-phase on the interior, iv) 25/75 bilayer with lower ϕ-phase on the interior, and v) linear sectioned-50/50 bilayer structure. First row displays as-printed structures, each subsequential row representing a ten minute delay, showing the shape alteration of the printed structures when immersed in water. Scale bar (bottom right) is 5 mm. The printed structures were left to swell for 3 h, the first 60 min are shown. b) $\epsilon_{max}^{H_2O}$ of 50/50 bilayer helices (radius = 7.5 mm, pitch = 15 mm, height = 60 mm) as a function of orientation of the bilayer cross-section relative to the center of rotation of the helical structure. 0° indicates that the low ϕ-phase is orientated toward the exterior of the helix, while 180° implies that it is placed toward the center of the helix. c) Swelling-induced extension is compared between helices (radius = 7.5 mm, pitch = 15 mm, height = 60 mm, printed with a bilayer structuring orientation of 180°) with varying ratios of low- and high ϕ-phases.

PEGDA ink. This filament lacks internal structure and swelling contrast, resulting in simple isotropic expansion with minimal geometry change. This homogeneous structure serves as a control and baseline for comparison. Comparing it to structures (ii), (iii), and (iv) highlights the substantial influence of internal bilayer patterning on shape alteration. When the 1.5 wt% PAA/10 wt% PEGDA and the 1.5 wt% PAA/20 wt% PEGDA hydrogels are sandwiched together in a bilayer, the contrast in the swelling and the difference in the swollen elasticity produces bending. In helical structures, if the lower ϕ-phase (10 wt% PEGDA ink) is oriented radially outward (structure (ii)), the printed structure contracts. Conversely, when the bilayer orients the phase with the highest swelling toward the center (structure (iii)), the helix elongates. The absorption of water by the 10 wt% PEGDA layer exerts stress on the 20 wt% PEGDA layer, causing dramatic unfolding of the helical structure. Figure 4a (v) shows a "sectioned bilayer" type of filament where the orientation of the bilayer is twisted 180° at regular intervals. This continuous macroscopically straight filament would likely be challenging to manufacture without the employment of a rotational printing setup. This straight filament contracts as a bent helix when exposed to water.

We quantify the *maximum structural swelling elongation* (in water) $\epsilon_{max}^{H_2O}$ by measuring the ratio between the end-to-end distance of printed objects before ($L_{initial}$) and after swelling in water for 180 min ($L_{swollen}$). We note that all analyzed structures reach between 87 and 95 % of the total equilibrium shape alteration after 60 min immersed in water.

$$\epsilon_{max}^{H_2O} = \frac{L_{swollen}}{L_{initial}} \tag{3}$$

We used $\epsilon_{max}^{H_2O}$ to evaluate actuation levels across different helical geometries and filament patterning. Initially, we compared $\epsilon_{max}^{H_2O}$ for helices with the same macroscopic dimensions (radius = 7.5 mm, pitch = 15 mm, height = 60 mm). These helices had symmetrical bilayer internal structures consisting of two inks with

© 2024 The Authors. Advanced Materials Technologies published by Wiley-VCH GmbH

different cross-linking densities: one composed of 1.5 wt% PAA + 10 wt% PEGDA, and the other composed of 1.5 wt% PAA + 20 wt% PEGDA. We examined the effect of bilayer orientation relative to the helix's center of rotation. Figure 4b shows the impact of a 0° bilayer orientation, with the lower ϕ-phase on the exterior of the helix (structure (ii) in Figure 4a). In water, this architecture shrank by approximately 36% ($\epsilon_{max}^{H_2O} < 1$) and a reduction in pitch and radius can be observed. Conversely, with the opposite bilayer orientation (structure (iii) in Figure 4a), the helix expanded by over 150% in water. Bilayer orientations between 0° and 180° induced progressively higher maximum elongation in the fully swollen state, as seen in the plot. Beyond 180°, this trend reversed. This series of experiments demonstrates how the rotational axis can be used as a handle to finely tune structure and subsequently actuation.

In a second series of experiments, while holding the bilayer orientation constant, we examined the impact of the relative thickness of the two phases within the bilayer, on the helical structures' swelling response (see Figure 4c). Maximum structural elongation was achieved when the two phases had equal thickness. Increasing the ratio of the 20 wt% PEGDA phase to the 10 wt% PEGDA phase within the helices significantly reduced the swelling response. This reduction was attributed to heightened helix rigidity and a reduced proportion of the more responsive 10 wt% PEGDA phase. An increase in the thickness of the 10 wt% PEGDA phase within the bilayer also led to a decrease in swelling response, though to a lesser extent.

The architecture that maximizes elongation during swelling is a 180° orientation and equal thickness of the low and high crosslinking density phase. Holding these parameters constant, we printed helices with radii ranging from 0 to 7.5 mm and pitches from 5 to 30 mm, while maintaining a constant structure height of 60 mm. The 3D plot in **Figure 5** illustrates the relationship between $\epsilon_{max}^{H_2O}$ after 180 min of immersion in water as a function of helical radius and pitch. A consistent pattern emerges: increasing the helical radius at a fixed pitch or decreasing the pitch at a fixed radius both result in greater structural elongation during swelling. However, for the largest radius (7.5 mm), an intermediate pitch produces the peak swelling response. The maximum elongation was observed in a bilayer helix with a 15 mm pitch and a 7.5 mm radius. While the mechanics of this swelling behavior are complex and beyond our current scope, the data underscores the impressive adjustability in these structures' shape morphing response, achieved by tuning basic fabrication parameters.

4. Conclusion

In this study, we developed a new 3D printing configuration that combines multi-material 3D printing, advective assembly, support bath 3D printing, and rotational axes to produce complex architectures that are impractical to produce via other means. The advective assembler nozzles build structures in laminar flows and extrude strong, multimaterial filaments, for example internally structured as to be made to be more resistant to potential delamination. The support bath allows the structured filaments to be arranged in curvilinear macroscopic shapes. Combining these distinct advances in additive manufacturing methods provides new spatial axes for design. Users can build composite materials without slicing architectures across X, Y, and Z dimensions.

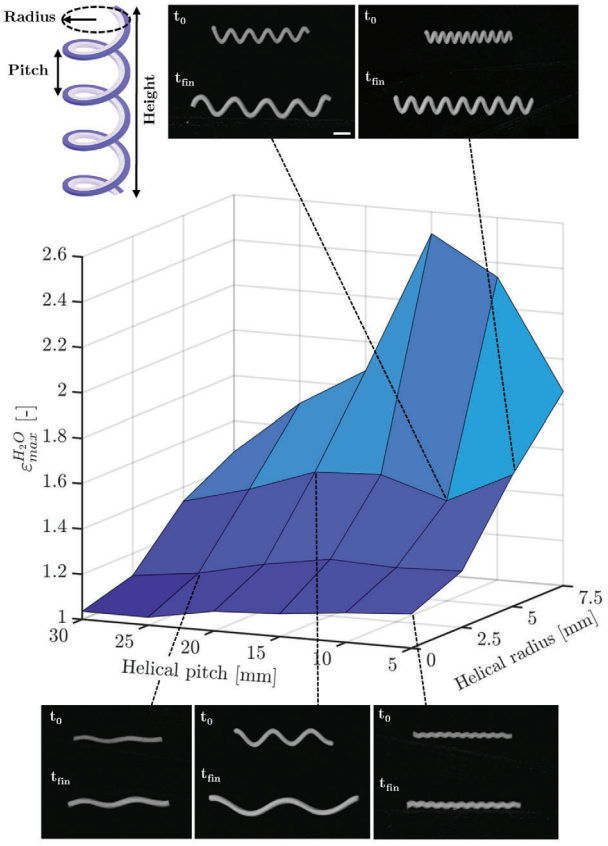

Figure 5. Effect of changing the pitch and radius of the helix. $\epsilon_{max}^{H_2O}$ for helical structures with a height of 60 mm, pitches varying between 5 and 30 mm and radii between 0 and 7.5 mm. Bilayer orientation is kept constant at 180°, and the ratio between the low and high ϕ-phase is set at 50/50.

To realize this printing platform, both the inks and the support bath were formulated to have a yield stress. We used PAA microgels in all formulations to modify rheology. For the support bath, we used a low 0.1 wt% PAA so that the bath could easily flow around and encase the printed structures, eventually supporting them against gravity. For the inks, we used a higher 1.5 wt% PAA to promote plug flow at reasonably high extrusion speeds. We performed linear and nonlinear bulk rheometry to provide benchmarks for those interested in formulating other materials for use with this process.

In this study, the PAA gels served as carrier for the polymeric monomers we wanted to precisely distribute throughout the printed object. The low molecular weight PEGDA can be UV cross-linked into a volume-spanning hydrogel. We co-flowed multiple inks with varying concentrations of PEGDA into the advective assembler printhead. The geometry of that printhead templates flow. We demonstrated how one printhead can be used to produce bilayers, stacked layers, and comb architectures by simply varying relative flow rates.

After the patterned filaments were extruded from the printhead, they were UV cross-linked to form hydrogels with patterned crosslinking density distributions. Each cross-linking density distribution is ordered over long range (e.g., 10 cm in height) with internal feature resolution on the order of 100s of μm. The

© 2024 The Authors. Advanced Materials Technologies published by Wiley-VCH GmbH

distributions curve smoothly and continuously in three dimensional space due to the combinations of the printing platform. The resolution limit of the internal features, for the specific case of the PAA-PEGDA hydrogel inks used, is influenced by the interdiffusion between phases before photo-polymerization. The interfaces between the regions with different PEGDA volume fraction diffuse, as in classic problems involving penetration depths. The sharpness of the gradient is affected by the total time of contact prior to polymerization. In processing terms, it is affected by both the residence time within the nozzle and the time between printing and UV polymerization.

We showcase the utility and adjustability of these designs by producing helical architectures, that could be interesting as soft hydrogel actuators.[50,51] Expansion, contraction, and bending are tuned with processing parameters such as flow rate, pitch, radius, and filament orientation. The internal structuring helps the relatively brittle hydrogels stay intact during extreme actuation strains.

With simple design knobs in hand, we can access a library of functional architectures using a single printing platform. We anticipate that even more gains are possible if this platform is used for other materials. The thorough rheological characterization of the ink and bath materials involved provide benchmarks to guide formulations of other materials. Since this printing process is inherently dictated by flow (in the nozzle, during extrusion, and of the encasing bath), we anticipate that materials with similar rheology can be incorporated seamlessly into this platform. Thus, advective-assembly-rotational-support-bath printing is a practical tool to architect composites over multiple length scales for improved performance.

Creating intricately controlled, hierarchically distributed structures poses significant challenges but is crucial for enhancing functionality in synthetic systems. While additive manufacturing has evolved, crafting complex unsupported 3D structures that combine diverse materials remains technically challenging and time-consuming. Our approach combines advective direct ink writing with support-bath rotational 3D printing for high-throughput fabrication of precisely designed multimaterial structures across different scales. This technology is adaptable to various materials, making it applicable in diverse fields, such as soft electronics, soft robotics or tissue engineering, where such multiphase monolithic hydrogel structures could help promote cell growth directionality.

5. Experimental Section

Materials: Poly(acrylic acid), powder (average Mw 4,000,000 g/mol; abbreviated as PAA) was purchased from Polysciences, Ink (Germany). Poly(ethylene glycol) diacrylate (average Mn 700 g/mol; abbreviated as PEGDA), 2-hydroxy-2-methylpropiophenone (97%; abbreviated as PI, for photo initiator), Triethanolamine (>99%, abbreviated as TEOA) and Chicago Sky Blue 6B Dye (abbreviated as Chicago Blue) were purchased from Sigma–Aldrich (Switzerland). Sodium Chloride (analytical reagent grade; abbreviated as NaCl) was purchased from Fisher Scientific (United Kingdom). The synthesis, chemical and fluorescence characterization of the dimethyl quinidinum acrylate, employed for the fluorescent visualization of concentration maps of the multiphase structures, are explained in details in the *Synthesis and Fluorescence of Dimethyl Quinidinium Acrylate* section of the Supporting Information, as this could be interesting to other researchers working with acrylic-based hydrogels.

Inks Preparation: Printable hydrogel inks were prepared by blending PAA microgels with various concentrations of PEGDA. 1.5 wt% PAA powder was mixed in Milli-Q H2O (Milli Q Advantage A10, resistivity: 18.2 MΩ ·cm, conductivity: 0.055 μScm^{-1}) by planetary centrifugal mixing (Thinky ARE-250, 10 min, 2000 RPM) and then mixed slowly but continuously over 24 h resulting in a homogeneous and viscous solution with a pH = 2.7 (Mettler Toledo S20 pH meter). Various amounts (10 and 20 wt% of the total solution) of PEGDA and PI (2 vol.% of PEGDA) were added to the solution and incorporated by planetary centrifugal mixing (10 min, 2000 RPM) resulting in a low viscosity, turbid solution. Chicago Blue dye was selectively added to the 20 wt% PEGDA solution to aid in visualization during advective processing. Dilute TEOA (molar ratio of 3:4 TEOA to acrylic acid groups) was added to the PAA-PEGDA solution by light planetary centrifugal mixing (3 min, 2000 RPM): this raises the pH from ≈3 to ≈7 resulting in ionization of the acrylic acid groups of the PAA microgels that swell to equalize osmotic pressure. For the fluorescent visualization of the concentration maps, 0.5 mmol of the dimethyl quinidinium acrylate was added to the 20 wt% PEGDA ink instead of the Chicago Blue dye. The fluorescent acrylate was added to the solutions only once a neutral pH was reached (after the addition of TEOA) in order to avoid any potential hydrolisis of the acrylic ester groups due to the acidic environment. The final hydrogel inks were loaded into syringes (Becton Dickinson Plastipak 30 mL syringes) and centrifuged (Hermle Z 206 A Centrifuge, 1 min, 3000 RPM) to remove bubbles.

Support Bath Preparation: Suspension bath solutions were prepared by mixing 0.1 wt% PAA powder in milli-Q H2O (planetary centrifugal mixing, 10 min, 2000 RPM). Unlike the inks, the low amount PAA fully dissolves easily in the water, hence no further homogenization steps were required. Dilute TEOA (molar ratio of 3:4 TEOA to acrylic acid groups) was then incorporated to the solution by light planetary centrifugal mixing (3 min, 2000 RPM). The solution could then be simply poured in the printing containers. Because of the relatively low viscosity and yield stress no air bubbles that would disrupt the printing process remain trapped in the suspension bath solution.

Rheological Characterization: Rheological measurements were performed using a controlled stress rheometer (Anton Paar, MCR 502) coupled with a Peltier temperature control unit set to 25.0 °C. Triplicate shear rate sweeps (Figure 2a) were performed from 0.01 to 100 s^{-1} in logarithmically spaced steps with durations varying from 200 to 10 s. A hatched 4°, 25 mm-diameter, 251 μm truncation gap, cone, and laser hatched bottom plate geometries were employed in these measurements in order to ensure homogeneous shear rates in the measuring geometry. Triplicate stress amplitude sweeps (Figure 2b) were measured with the same hatched 4°, 25 mm-diameter,251 μm truncation gap, cone, and laser hatched bottom plate geometries at a angular frequency of ω = 10 rads^{-1}. The dynamic yield stress ($\tau_{y,\,dynamic}$) and was calculated as the shear stress value corresponding to when the measured storage modulus drops below 90% of its linear viscoelastic region (LVE) plateau value.[52] 3ITT (see Figure S3c, Supporting Information) and printhead's analysis of shear conditions (Figure 2c (ii)) were performed using smooth 25 mm diameter parallel plates geometries in order to better replicate the shearing conditions in the smooth printhead channels, at a measuring gap of 1 mm. Shear rate sweeps measurements were repeated with smooth 25 mm diameter parallel plates geometries on a same sample at gap heights of 0.6, 0.8, 1.2, and 1.4 mm to rule out the presence of slip in the measurements (see Figure S4a, Supporting Information). To assess if averaging windows were long enough for the samples to reach steady state during the shear rate sweeps, shear stress was measured over eight separate 1000 seconds-long constant shear rate steps, logarithmically spaced between 0.01 and 50 s^{-1}. Between each constant shear rate step the sample was allowed to come to rest for 180 s. The tool, sample and a sponge saturated with water were enclosed in a solvent trap in order to avoid dehydration of the hydrogels during the 160 min-long measurement. The terminal shear stress value was extrapolated as an average of the shear stress measured over the last 800 s of each shear rate step (see Figure S4b, Supporting Information). Comparing these extrapolated values with an average shear rate sweep (triplicate measurements) confirms that the variable averaging windows employed in the shear rate

© 2024 The Authors. Advanced Materials Technologies published by Wiley-VCH GmbH

sweeps were long enough to allow the samples to reach steady state (see Figure S4c, Supporting Information).

Printhead Fabrication: The flow-structuring printhead was designed in Autodesk Inventor Professional 2023 and printed on a SLA 3D printer (Formlabs Form 3, clear v4 resin, adaptive layers height).

Printing and Post-Processing: Ink-loaded syringes were mounted on up to four syringe pumps (HA Harvard Apparatus, pump 11 Elite,standard infuse/withdraw programmable syringe pumps, 155.7 N maximum linear force, 1.26 $pLmin^{-1}$ - 26.02 $mLmin^{-1}$ flow rates range) that allow for precise and independent control over volumetric flow rates and connected to the advective-assembler printhead with PVC tubing (Semadeni transparent PVC-P, 3 mm ID, 5 mm OD). A total flow rate of 540 $\mu lmin^{-1}$ was used for all printing experiments. A commercial E3D Tool-Changer (E3D-online, UK) was modified to accommodate the custom printhead, that was secured to the removable E3D ToolPlate using screws, and allowed for control over x, y, and z-axis position of the flow-structuring nozzle. For most of the printing experiments the suspension bath solution was contained in a 50 mL SARSTEDT (Switzerland) conical base centrifuge tube and fixed to a rotating motor with a custom 3D-printed adapter. The printing path was controlled with custom G-code routines, that defined x, y, z movement and speed, and suspension bath rotation. Once the printing procedure was finished, and the structured filaments were suspended in the bath, they were quickly photopolymerized for 90 s (Gie-Tec, UV Exposure Box 2, AC 230 V, 50–60 Hz, 60 VA, $\lambda = 365$ nm). The cross-linked structures could at this point be removed by hand from the suspension bath, which could be reused.

Imaging Shape Transformation of the Printed Structures upon Differential Swelling: The printed, polymerized multi-phase structures undergo a small degree of swelling after photopolymerization and prior to being removed from the suspension bath, because of the extremely high content of water in the suspension bath. Because of this reason, prior to recording their shape alteration due to swelling, they were placed in a 1M NaCl solution for 1 h in order to ensure that when recording, their shape alteration starts from the configuration imposed by the 3D-printing procedure. The printed structures were then placed in a 20 cm by 20 cm glass tank filled with deionized water, their shape alteration upon differential swelling of the differently crosslinked internal phases was recorded (Dino Elite Edge, Digital Microscope) over the course of 180 min. End-to-end elongation was extracted with ImageJ.

Fluorescent Visualization of Concentration Maps: The Chicago Blue dye was helpful to visualize the inks flow in the printhead and in the suspension bath, but this was quickly bleached during the photopolymerization step, and cannot be employed to visually distinguish the different arrangement of phases in the cross-linked filaments. PAA-PEGDA ink containing the dimethyl quinidinium acrylate was used to image the cross sectional geometry of the multiphase filaments (see Figure 3). The dimethyl quinidinium acrylate was added to the 20 wt% PEGDA ink, this fluorophore emits at $\lambda = 365$ nm (fluorescence characterization is displayed in Figures S10 and S11, Supporting Information). The fluorophore-modified ink was employed in order to image the position and diffusion of the two phases in the cross-linked filaments. Filaments were printed as explained before. After photopolymerization, the filaments were frozen in liquid nitrogen and sliced with a razor blade sharpened as a chisel. Cutting the filaments in the solid frozen state reduces the formation of cracks on the patterned filament surface (that would diffract the fluorescence emission during imaging and mess up the precise detection of the phases). Furthermore, the chiseled and polished razor blade prevents microstreaks on the cleaved filament faces. Filaments were cut into 0.5 – 1 mm thick slices and imaged on a fluorescent microscope (Nikon Eclipse Ti, illumination CoolLED PE 4000 at $\lambda = 365$ nm, Hamamatsu CMOS camera, 300 ms exposure). A heat map of the relative fluorophore concentration in the PAA-PEGDA phases was scaled according to the imaged signal intensity.

Supporting Information

Supporting Information is available from the Wiley Online Library or from the author.

Acknowledgements

This work was supported by the ETH domain, Strategic Focus Area Advanced Manufacturing (SFA AM) project MANUFHAPTICS, and the authors thank Prof. Herbert Shea (EPFL), Prof. Dorina Opris (EMPA) and Prof. André Studart (ETHZ) for stimulating discussions. The authors would also like to thank Dr. Stephan Busato for his help in the synthesis and characterization of the dimethyl quinidinium acrylate and Lucas Bidoire for his help in the fluorescent imaging of the multi-phase filaments' cross-sections. The authors also acknowledged Dr. Kirill Fishman Feldman for his help across different phases of the practical work in the laboratory.

Open access funding provided by Eidgenossische Technische Hochschule Zurich.

Conflict of Interest

The authors declare no conflict of interest.

Data Availability Statement

The data that support the findings of this study are available in the supplementary material of this article.

Keywords

additive manufacturing, advective assemblers, direct ink writing, rheology, rotational 3d printing, support bath

Received: January 2, 2024
Revised: March 26, 2024
Published online:

[1] B. Wang, W. Yang, J. McKittrick, M. A. Meyers, *Prog. Mater. Sci.* **2016**, *76*, 229.
[2] U. Kutschera, *Physiol. Plant.* **1989**, *77*, 157.
[3] M. J. Harrington, K. Razghandi, F. Ditsch, L. Guiducci, M. Rueggeberg, J. W. Dunlop, P. Fratzl, C. Neinhuis, I. Burgert, *Nat. Commun.* **2011**, *2*, 337.
[4] J. Cesarano, S. Grieco, *Mater. Technol.* **1997**, *12*, 98.
[5] A. Shahzad, I. Lazoglu, *Compos. B Eng.* **2021**, *225*, 109249.
[6] A. M'Barki, L. Bocquet, A. Stevenson, *Sci. Rep.* **2017**, *7*, 6017.
[7] J. A. Lewis, *Adv. Funct. Mater.* **2006**, *16*, 2193.
[8] S. Colanges, J.-N. Tourvieille, P. Lidon, J. Leng, *Sci. Rep.* **2023**, *13*, 5155.
[9] C. Xu, B. Quinn, L. L. Lebel, D. Therriault, G. L'Espérance, *ACS Appl. Mater. Interfaces* **2019**, *11*, 8499.
[10] V. C.-F. Li, X. Kuang, C. M. Hamel, D. Roach, Y. Deng, H. J. Qi, *Addit. Manuf.* **2019**, *28*, 14.
[11] T. J. Hinton, A. Hudson, K. Pusch, A. Lee, A. W. Feinberg, *ACS Biomater. Sci. Eng.* **2016**, *2*, 1781.
[12] M. Stang, J. Tashman, D. Shiwarski, H. Yang, L. Yao, A. Feinberg, *Adv. Mater. Technol.* **2023**, *8*, 2200984.
[13] O. Jeon, Y. B. Lee, H. Jeong, S. J. Lee, D. Wells, E. Alsberg, *Mater. Horiz.* **2019**, *6*, 1625.
[14] F. Afghah, M. Altunbek, C. Dikyol, B. Koc, *Sci. Rep.* **2020**, *10*, 1.
[15] Y. Guo, Y. Liu, J. Liu, J. Zhao, H. Zhang, Z. Zhang, *Compos. - A: Appl. Sci. Manuf.* **2020**, *135*, 105903.
[16] A. Renteria, V. H. Balcorta, C. Marquez, A. A. Rodriguez, I. Renteria-Marquez, J. Regis, B. Wilburn, S. Patterson, D. Espalin, T.-L. B. Tseng, Y. Lin, *Flex. Print. Electron.* **2022**, *7*, 015001.

© 2024 The Authors. Advanced Materials Technologies published by Wiley-VCH GmbH

[17] P. M. Danner, T. Pleij, G. Siqueira, A. V. Bayles, T. Raman Venkatesan, J. Vermant, D. M. Opris, *Adv. Funct. Mater.* **2023**, *34*, 2313167.
[18] F. Chen, Z. An, Y. Chen, Y. Li, X. Liu, N. Chen, Y. Ru, D. Gao, *Chem. Eng. J.* **2023**, *471*, 144770.
[19] T. B. Palmić, J. Slavič, *Int. J. Mech. Sci.* **2022**, *230*, 107555.
[20] D. Kokkinis, F. Bouville, A. R. Studart, *Adv. Mater.* **2018**, *30*, 1705808.
[21] I. Hassan, P. R. Selvaganapathy, *Addit. Manuf.* **2022**, *50*, 102559.
[22] C. J. Hansen, R. Saksena, D. B. Kolesky, J. J. Vericella, S. J. Kranz, G. P. Muldowney, K. T. Christensen, J. A. Lewis, *Adv. Mater.* **2013**, *25*, 96.
[23] J. O. Hardin, T. J. Ober, A. D. Valentine, J. A. Lewis, *Adv. Mater.* **2015**, *27*, 3279.
[24] W. Liu, Y. S. Zhang, M. A. Heinrich, F. De Ferrari, H. L. Jang, S. M. Bakht, M. M. Alvarez, J. Yang, Y.-C. Li, G. Trujillo-de Santiago, A. K. Miri, K. Zhu, P. Khoshakhlagh, G. Prakash, H. Cheng, X. Guan, Z. Zhong, J. Ju, G. H. Zhu, X. Jin, S. R. Shin, M. R. Dokmeci, A. Khademhosseini, *Adv. Mater.* **2017**, *29*, 1604630.
[25] M. A. Skylar-Scott, J. Mueller, C. W. Visser, J. A. Lewis, *Nature* **2019**, *575*, 330.
[26] Y. S. Zhang, Q. Pi, A. M. Van Genderen, *J. Vis. Exp.* **2017**, *126*, e55957.
[27] F. Feng, J. He, J. Li, M. Mao, D. Li, *Int. J. Bioprinting* **2019**, *5*, 202.
[28] A. Chortos, J. Mao, J. Mueller, E. Hajiesmaili, J. A. Lewis, D. R. Clarke, *Adv. Funct. Mater.* **2021**, *31*, 22.
[29] N. M. Larson, J. Mueller, A. Chortos, Z. S. Davidson, D. R. Clarke, J. A. Lewis, *Nature* **2023**, *613*, 682.
[30] L. Ren, W. Li, H. Liu, B. Li, X. Zhou, L. Ren, Z. Han, Z. Song, Q. Liu, *Addit. Manuf.* **2023**, *73*, 103661.
[31] R. Schaller, P. E. Neerincx, H. E. Meijer, *Macromol. Mater. Eng.* **2017**, *302*, 6.
[32] P. E. Neerincx, M. Hofmann, O. Gorodetskyi, K. Feldman, J. Vermant, H. E. Meijer, *Polym. Eng. Sci.* **2021**, *61*, 1257.
[33] P. E. Neerincx, R. P. Denteneer, S. Peelen, H. E. Meijer, *Macromol. Mater. Eng.* **2011**, *296*, 349.
[34] H. E. Meijer, M. K. Singh, P. D. Anderson, *Prog. Polym. Sci.* **2012**, *37*, 1333.
[35] P. E. Neerincx, H. E. H. Meijer, *Macromol. Chem. Phys.* **2013**, *214*, 188.
[36] A. V. Bayles, T. Pleij, M. N. Murdock, J. Vermant **2024 (unpublished)**.
[37] A. V. Bayles, T. Pleij, M. Hofmann, F. Hauf, T. Tervoort, J. Vermant, *ACS Appl. Mater. Interfaces* **2022**, *14*, 15667.
[38] C. Miller, *Ind. Eng. Chem. Fund.* **1972**, *11*, 524.
[39] S. Curran, R. Hayes, A. Afacan, M. Williams, P. Tanguy, *J. Food Sci.* **2002**, *67*, 176.
[40] M. R. Sommer, M. Schaffner, D. Carnelli, A. R. Studart, *ACS Appl. Mater. Interfaces* **2016**, *8*, 34677.
[41] G. Siqueira, D. Kokkinis, R. Libanori, M. K. Hausmann, A. S. Gladman, A. Neels, P. Tingaut, T. Zimmermann, J. A. Lewis, A. R. Studart, *Adv. Funct. Mater.* **2017**, *27*, 1604619.
[42] J. T. Muth, D. M. Vogt, R. L. Truby, Y. Mengüç, D. B. Kolesky, R. J. Wood, J. A. Lewis, *Adv. Mater.* **2014**, *26*, 6307.
[43] T. Bhattacharjee, S. M. Zehnder, K. G. Rowe, S. Jain, R. M. Nixon, W. G. Sawyer, T. E. Angelini, *Sci. Adv.* **2015**, *1*, e1500655.
[44] A. K. Grosskopf, R. L. Truby, H. Kim, A. Perazzo, J. A. Lewis, H. A. Stone, *ACS Appl. Mater. Interfaces* **2018**, *10*, 23353.
[45] S. Timoshenko, *J. Opt. Soc. Am.* **1925**, *11*, 233.
[46] E. Reyssat, L. Mahadevan, *J. R. Soc., Interface* **2009**, *6*, 951.
[47] G. Gao, L. Wang, Y. Cong, Z. Wang, Y. Zhou, R. Wang, J. Chen, J. Fu, *ACS Omega* **2018**, *3*, 17914.
[48] G. Gao, Z. Wang, D. Xu, L. Wang, T. Xu, H. Zhang, J. Chen, J. Fu, *ACS Appl. Mater. Interfaces* **2018**, *10*, 41724.
[49] T. M. Valentin, E. M. Dubois, C. E. Machnicki, D. Bhaskar, F. R. Cui, I. Y. Wong, *Polym. Chem.* **2019**, *10*, 2015.
[50] Y. Lee, W. Song, J.-Y. Sun, *Mater. Today Phys.* **2020**, *15*, 100258.
[51] Y. Chen, Y. Zhang, H. Li, J. Shen, F. Zhang, J. He, J. Lin, B. Wang, S. Niu, Z. Han, Z. Guo, *Nano Today* **2023**, *49*, 101764.
[52] J. Mewis, N. J. Wagner, *Colloidal Suspension Rheology*, 1 edition, Cambridge University Press, Cambridge **2011**.

© 2024 The Authors. Advanced Materials Technologies published by Wiley-VCH GmbH